

A study on Ca II 854.2 nm emission in a sunspot umbra using a thin cloud model

H. Hamedivafa¹ · M. Sobotka² · L. Bellot Rubio³ · S. Esteban Pozuelo^{4,3}

¹ Physics Department, Faculty of Science, Imam Khomeini International University, Qazvin 34149-16818, Islamic Republic of Iran; email: vafa@sci.ikiu.ac.ir

² Astronomical Institute, Academy of Sciences of the Czech Republic (v.v.i.), Fričova 298, CZ25165 Ondřejov, Czech Republic; email: michal.sobotka@asu.cas.cz

³ Instituto de Astrofísica de Andalucía (CSIC), Apdo. 3004, 18080 Granada, Spain; email: lbellot@iac.es

⁴ Institute for Solar Physics, Department of Astronomy, Stockholm University, AlbaNova University Center, 106 91 Stockholm, Sweden; email: sara.esteban@astro.su.se

Abstract. In the present work, we introduce and explain a method of solution of the radiative transfer equation based on a thin cloud model. The efficiency of this method to retrieve dynamical chromospheric parameters from Stokes I profiles of Ca II 854.2 nm line showing spectral emission is investigated. The analyzed data were recorded with the Crisp Imaging Spectro-Polarimeter (CRISP) at Swedish 1-m Solar Telescope on La Palma on 2012 May 5 between 8:11 - 9:00 UT. The target was a large decaying sunspot (NOAA 11471) at heliocentric position W 15° S 19°. This sunspot has a large umbra divided into two umbral cores (UCs). One of these UCs shows steady spectral emission in both Ca II 854.2 nm and H α lines, where downflows prevail. The other UC shows intermittent spectral emission only in Ca II 854.2 nm, when umbral flashes are propagating. The statistics of the obtained Doppler velocities in both UCs is discussed.

Keywords: Sun: sunspots

1 Introduction

The sunspot chromosphere comprises a number of inhomogeneously magnetized plasma features relevant to flows, waves, shocks. These dynamical features affect the spectral absorption and emission characteristics of the chromosphere of sunspots.

One of these dynamical features, an umbral flash (UF), is a sudden brightening observed in the chromospheric core of the Ca II lines. UFs tend to appear with a periodicity of roughly 3 min [1, 2, 3]. It seems that they are the chromospheric counterpart of the photospheric oscillation and are connected to the phenomenon known as running umbral/penumbral waves (for a review see [4]).

By LTE and non-LTE inversions using spectro-polarimetric Ca II 854.2 nm observations, de la Cruz Rodríguez et al. [5] confirmed that UFs have very fine structure with hot and cool material intermixed at sub-arcsecond scales. They have found a temperature excess of about 1000 K and upflows of 4 km s⁻¹ around the temperature minimum region. The corresponding 2D temperature maps have shown a hot canopy above the umbra during UFs, which was not observed in quiet phases. This canopy coincides with areas showing enhanced line-core emission.

The first polarimetric observations of UFs [2, 6] already revealed the occurrence of “anomalous” Stokes V profiles during the UF events. Socas-Navarro et al. [2, 6] explained anomalous profiles by a two-component scenario: an unresolved mixture in the horizontal

direction where a certain filling factor is occupied by a “quiet” component (no reversal and zero or slightly downflowing velocity), while the rest is occupied by the shock-wave (line core emission reversal and strong upflows).

Besides inversions based on one-, two- or multi-component models, “cloud model” represents an alternative spectral inversion technique describing the transfer of radiation through cloud-like structures located above the “solar surface”, transmitting the radiation coming from below according to their optical thickness and source function. Beckers [7] introduced a simple inversion technique, known in the literature as “Beckers’ cloud model”, for inferring the physical parameters of the cloud. Different solutions of the radiative transfer equation based on the cloud model were reviewed by Tziotziou [8]. The cloud-model method is much simpler than the complete calculation of a model atmosphere based on the non-LTE inversion of chromospheric spectral lines and it seems to be suitable for our purpose. The presence of the hot canopy with line-core emission detected in [5] during UFs, i.e., a kind of cloud-like structure, indicates that the cloud-model approach is viable.

We intend to obtain Doppler velocities in the chromosphere above a sunspot umbra where we observe signatures of UFs (spectral emissions) in the Ca II 854.2 nm line using a suitable cloud model describing umbral chromosphere. The cloud model provides a good representation of the observed profiles and a reliable quantitative description of the spatial distribution of the physical parameters responsible for the observed intensity inhomogeneities formed in the body of the cloud structure [9, 10].

The paper is arranged as follows: the data sets are described in Sect. 2. A general description of the chromospheric spectral emissions observed in our data sets is provided in Sect. 3. A detailed description of the cloud model and a method to solve the radiative transfer equation based on a new idea are provided in Sect. 4. In Sect. 5 we describe the results and the reliability of the obtained model parameters. Finally, we summarize our conclusions in Sect. 6.

2 Data Set

The data analyzed in this study were recorded with the Crisp Imaging Spectro-Polarimeter (CRISP; [11]) at the Swedish 1-m Solar Telescope (SST; [12]) on La Palma. The dataset includes the simultaneous sequences of full Stokes profiles of Ca II infrared line at 854.2 nm, Fe I at 617.3 nm, and the Stokes I in $H\alpha$ acquired on 2012 May 5 between 8:11 - 9:00 UT (49 min). The target was a large decaying sunspot (NOAA 11471) at heliocentric position W 15° S 19° equivalent to the heliocentric angle of 23 deg ($\mu = 0.92$).

Data reduction was performed using the CRISPRED pipeline described in [13]. The Ca II 854.2 nm observations are affected by a backscatter problem. The CRISP acquisition system has three back-illuminated Sarnoff cameras. Their quantum efficiency decreases in the infrared wavelengths and, above approximately 700 nm, each CCD camera becomes partially transparent. Consequently, images acquired at Ca II 854.2 nm show a circuit pattern that cannot be removed using standard dark and flat field corrections. To solve this problem, the flat field process of the Ca II 854.2 nm was performed considering the aspects discussed in [5].

The dataset consists of a time series of profile scans of the mentioned three spectral lines with a cadence of 56.5 s (52 scans). The Ca II line was observed at 17 line positions with a sampling of 0.01 nm between $\Delta\lambda = \pm 0.08$ nm along with a continuum sample at $\Delta\lambda = +0.24$ nm. The profile scans of Fe I line are sampled at 31 wavelengths ranging between $\Delta\lambda = -30.8$ pm and $\Delta\lambda = +53.2$ pm around the line center at 2.8 pm spacing. The scans of Stokes I profiles of $H\alpha$ line are sampled at 21 wavelengths ranging between

$\Delta\lambda = \pm 0.1$ nm around the line center with 0.01 nm spacing. The formation height of the iron line is in the photosphere while both Ca II 854.2 nm and H α are chromospheric spectral lines, the former being formed at higher layers [14]. According to Cauzzi, et al. [14], the wings of Ca II infrared line are formed in the middle photosphere while its core comes from the middle chromosphere. After data reductions and the co-aligning the scans of different spectral lines, the FOV is reduced to 830×865 pixels ($49'' \times 51''$).

3 General Properties and Chromospheric Emission

Fig. 1 shows simultaneous filtergrams of these three spectral lines. In the photosphere, observed in Fe I continuum (top-left panel), the granulation pattern surrounds the observed irregular sunspot. The sunspot contains a big umbra and a tail containing a few umbral cores.

A filamentary light-bridge divides the big umbra in two halves. The Ca II continuum image (top-right panel) shows similar structures as well as bright filigree in the surrounding granulation. At $\Delta\lambda = \pm 0.03$ nm away of the expected line center of Ca II line, we can see its chromospheric contribution (the middle-row panels). The superpenumbra is seen in the line core images (the bottom row panels). The white box shown in panels of Fig. 1 encloses the region, the big umbra, where we study the chromospheric spectral emission in Ca II 854.2 nm.

As can be seen in top row of Fig. 2, the upper half of the big umbra shows bright dot-like structures in near-red wing filtergrams. Near-blue wing filtergrams, bottom row of Fig. 2, do not clearly show such bright dot-like structures (smeared bright structures with lower contrast are observed instead). When we get closer to the line core (see middle row of Fig. 2), we can see the chromosphere. Then, these dot-like structures are changing to a continuous bright structure (a bright cloud) which is steadily seen during the whole observation so that we could not recognize the upper half of the umbra from its adjacent penumbra. Also, the steady bright cloud is obviously seen in H α filtergrams (see bottom-left panel in Fig. 1).

Running waves and umbral flashes are seen moving inside the big umbra and in the tail of umbral cores as well and passing the penumbra in the time series of line-core and near blue-wing filtergrams of Ca II line (see middle and bottom rows of Fig. 2). Near red-wing filtergrams of Ca II do not clearly show signatures of umbral flashes.

The bright cloud seen in the chromosphere of the upper half of the big umbra is a signature of steadily strong emissions in both Ca II and H α spectral lines in this part of the umbra. Fig. 3 shows samples of Stokes I profiles of the observed spectral lines at two pixels in the big umbra, pixel **a** in the lower half umbra (*quiet umbra*) and pixel **b** in the upper half umbra (*active umbra*), as well as at pixel **c** in the surrounding granulation. These three pixels are marked as **a**, **b** and **c**, respectively, in Fig. 1.

In the quiet umbra, the Ca II line shows emission signature when umbral flashes are passing through the umbra while the H α line shows a blue-shifted absorption profile. However, active umbra shows steady and strong spectral emissions in both Ca II and H α lines, irrespective of evolving umbral flashes. Nevertheless, running waves and umbral flashes only slightly and temporarily change the brightness of the bright cloud in the line-core filtergrams (see middle row of Fig. 2) which is essentially because of the effect of the Doppler shift of the emission part of the line profile. Also, umbral flashes and the resulting Doppler-shifted emission part of the profiles can change more conspicuously the shape and brightness of the bright cloud at the near-wing filtergrams (see top and bottom rows in Fig. 2).

As can be seen in Fig. 3, the Stokes I profile of the Ca II line for pixel **a** shows a conspicuous emission in the blue wing, while the Stokes I profile of H α line shows a blue-

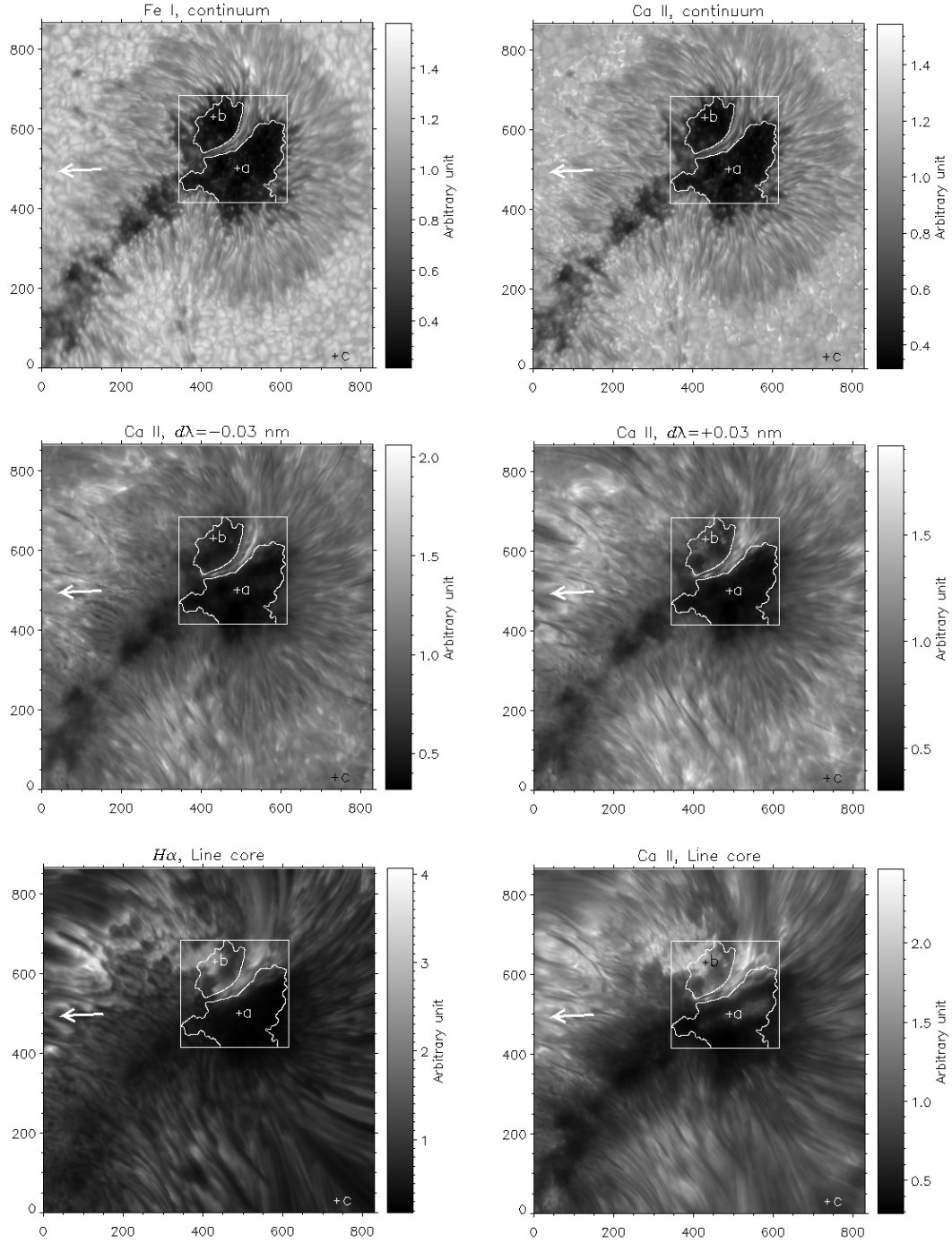


Figure 1: Illustrations of filtergrams of three spectral lines (the fourth scan). Top-left panel: Fe I continuum at $\Delta\lambda = +0.05$ nm. Top-right panel: Ca II continuum at $\Delta\lambda = +0.24$ nm. Middle panels: Ca II filtergrams at $\Delta\lambda = \pm 0.03$ nm. Bottom-left panel: line-core image of $H\alpha$. Bottom-right panel: line-core image of Ca II. The white arrow points to disk center. The white box encloses the big umbra: the region where we study the chromospheric spectral emission. Pixels *a*, *b* and *c* are adopted to represent the two parts of the umbra and a surrounding granulation.

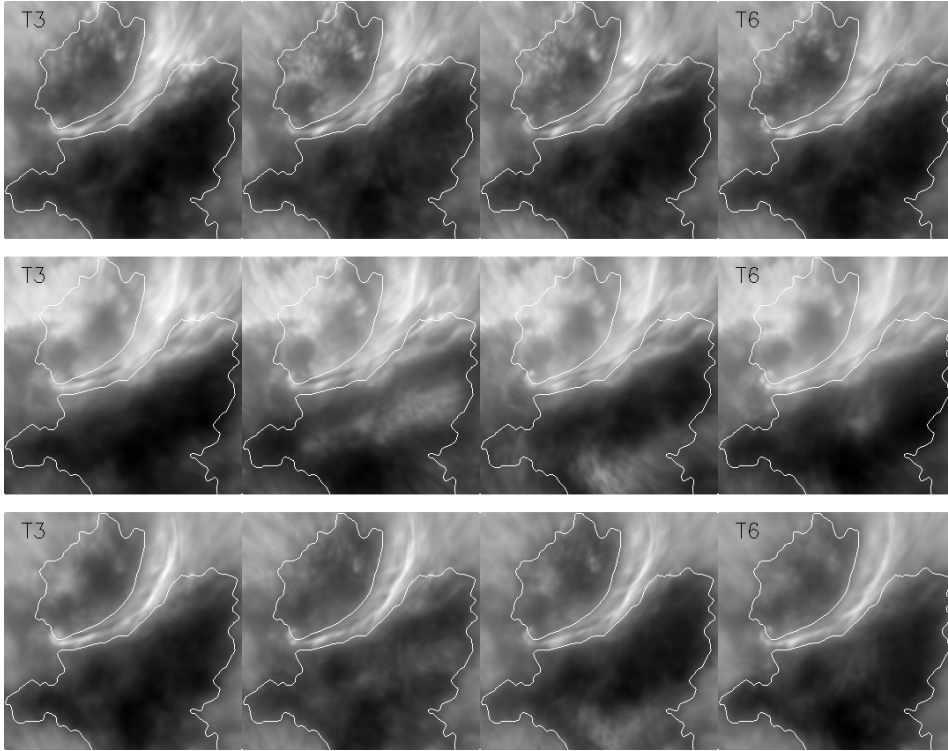


Figure 2: Four successive intensity filtergrams of the Ca II line, from the third scan through the sixth scan. Top row: near red-wing ($\Delta\lambda = +0.03$ nm) filtergrams. Middle row: line-core filtergrams. Bottom row: near blue-wing ($\Delta\lambda = -0.03$ nm) filtergrams. Time is elapsing from left to right. All images in each row were displayed with the same logarithmic scaling. White contours enclose the active and quiet umbra as in Fig. 1. The size of each map is 270×270 pixels ($16'' \times 16''$)

shift and a deformation in its red wing. Also, this deformation is seen in the red wing of Stokes I of pixel c (see bottom panel of Fig. 3). To have a detailed comparison, Fig. 4 displays eight successive Stokes I profiles of Ca II and $H\alpha$ for pixel a . We can see a correlation between the occurrence of emission in the Ca II line and a global blue-shift in the $H\alpha$ profile along with a deformation in its red wing. There are two exceptions in the first row panels for dash-dotted and dash-triple dotted lines: They show a time delay between emission signatures in the Ca II line and the global blue shift in $H\alpha$ line maybe because of the time difference between the Ca II and $H\alpha$ scans. The observed deformation in the red wing of the Stokes I of $H\alpha$ line can be a signature of velocity gradients connected with the oscillations. The inequality of the blue and red continua of the $H\alpha$ line is probably caused by weak absorption lines of Co I and atmospheric H_2O in the region 656.34 - 656.42 nm.

Fig. 5 illustrates temporal changes (λ - t diagrams) of $H\alpha$ Stokes I and Ca II (Stokes I and V). The Ca II line shows discrete emissions, corresponding to umbral flashes, in pixel a (quiet umbra, left panel) and a steady emission in pixel b (active umbra, right panel), where umbral flashes are also seen. The “polarity reversal” (a reversed sign not a true polarity reversal) in Ca II Stokes V occurs when a strong emission appears. Pixel b shows a steady reversed polarity sign with time-varying Doppler shifts. In the quiet umbra, the $H\alpha$ line

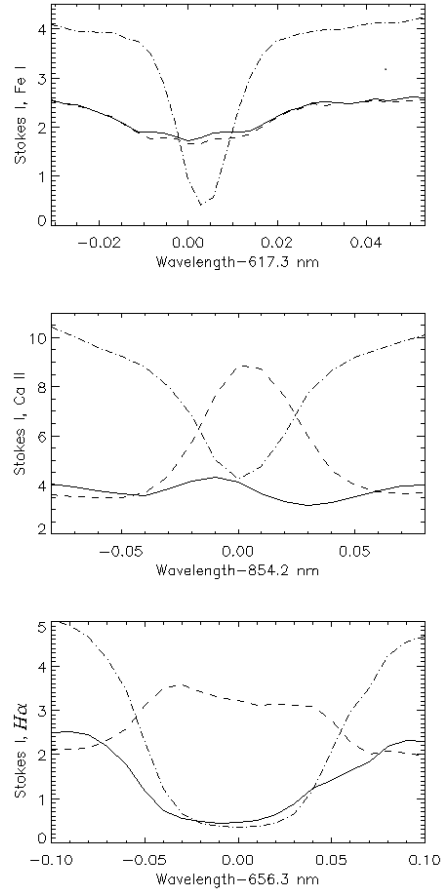


Figure 3: Examples of Stokes I of Fe I (top panel), Ca II (middle panel) and H α (bottom panel) lines at the pixel **a** in the quiet umbra (solid lines), pixel **b** in the active umbra (dashed lines) and pixel **c** in the surrounding granulation (dash-dotted lines). For a better visualization, the Stokes I of pixel **c** in top panel was shifted down by 5 units and the Stokes I of pixel **c** in bottom panel was divided by 3. All profiles were extracted from the third scan.

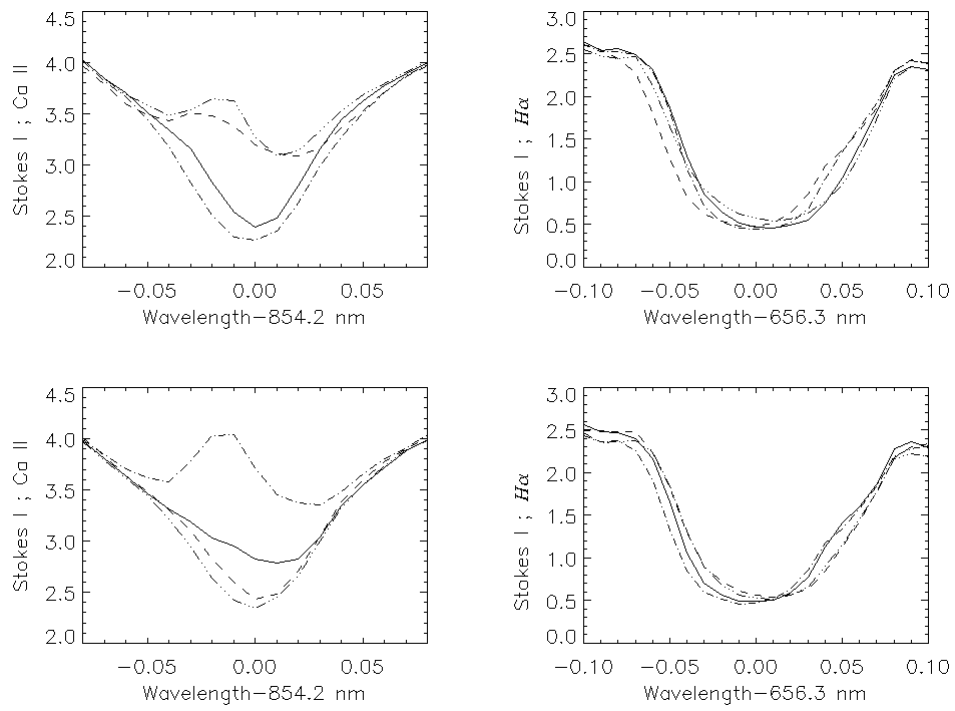


Figure 4: First row: four successive Stokes I profiles of Ca II (left panel) and $H\alpha$ (right panel) for pixel a in quiet umbra. Second row: the next four successive Stokes I profiles the same as the first row. Time is elapsing through solid, dashed, dash-dotted and dash-triple-dotted lines.

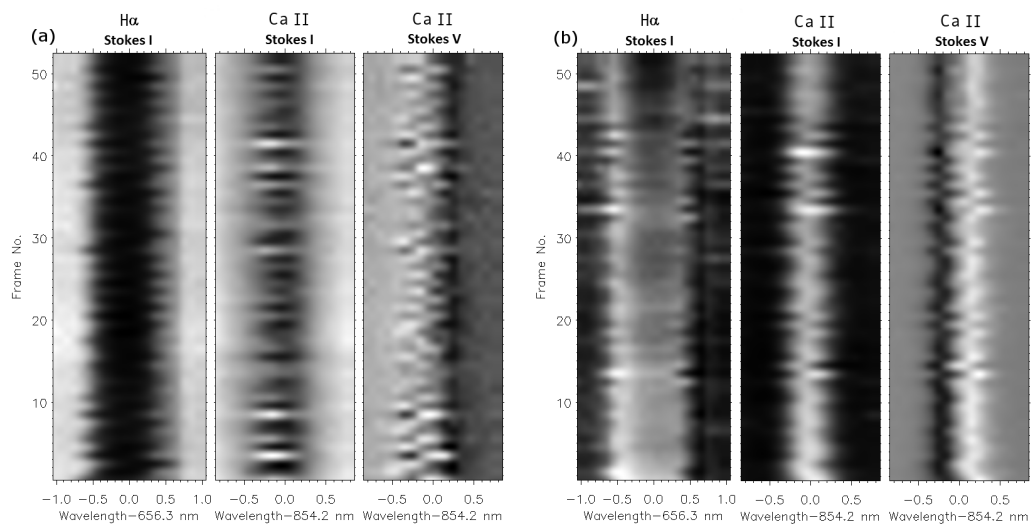


Figure 5: Temporal changes of H α (Stokes I) and Ca II (Stokes I and V) in pixel a (left panel) and pixel b (right panel).

has an absorption profile while in the active umbra, H α is steadily in emission. Both the absorption and emission profiles show blue-shifts and asymmetries during umbral flashes.

4 The Cloud Model

The aim of this paper is to study Doppler velocities in the chromosphere above the umbra where we observe emission signatures in the Ca II line.

Spectral inversion techniques based on cloud model [8] are extremely useful for the study of properties and dynamics of various chromospheric cloud-like structures.

Cloud models refer to models describing the transfer of radiation through structures located above the solar photosphere. Such cloud-like structures seem to absorb the incident radiation coming from below and to add some emissions. The mentioned absorption and emission processes are described by the formal solution of the radiative transfer equation

$$I_\lambda = I_{0\lambda}e^{-\tau_\lambda} + \int_0^{\tau_\lambda} S_t e^{-t_\lambda} dt_\lambda \quad (1)$$

where I_λ is the observed intensity, $I_{0\lambda}$ is the incident radiation to the cloud from below, τ_λ is the optical thickness and S_t is the source function which can be a function of optical depth inside the cloud. The first term of the right hand part of the Eq. (1) represents the absorption of the incident radiation by the cloud while the second term represents the added emission by the cloud itself.

4.1 Thin Cloud Model

We follow the Beckers cloud model [7] by assuming that **a)** the source function and the LOS velocity are constant through the whole cloud, **b)** the optical thickness of the cloud has a Gaussian wavelength dependence with a constant Doppler width, and more important, **c)** the cloud is optically thin to produce a strong emission superimposed on an absorption profile. Heinzel and Schmieder [15], using a grid of many non-LTE models of prominence-like structures, found that a constant source function corresponds to a low-pressure, optically thin structure. Fig. 6 shows the geometry of the cloud in the solar atmosphere; the cloud can be defined as upper layers of umbral chromosphere that are optically thin. There must be an active mechanism inside these layers producing a strong emission.

By these considerations, Eq. (1) is reduced to

$$I_\lambda = I_{0\lambda} - \tau_\lambda I_{0\lambda} + \tau_\lambda S \quad (2)$$

The third term on the right hand side of Eq. (2) $E_\lambda = \tau_\lambda S$ is the added total emission term that can be interpreted as the wavelength-dependent total emission of the cloud. This means that we do expect that a profile showing emission is described by the product $\tau_\lambda S$, not by S and τ_λ separately. Eq. (2) can be rewritten as

$$I_\lambda = I_{0\lambda} + \tau_\lambda(S - I_{0\lambda}) \quad (3)$$

The optical thickness of the cloud is described by a Gaussian function as

$$\tau_\lambda = \tau_0 e^{-\left(\frac{\lambda - \lambda_P}{W}\right)^2} \quad (4)$$

where τ_0 ($\ll 1$: cloud is optically thin) is the peak optical thickness, W is the Doppler width and λ_P is the Doppler shifted wavelength of the peak absorption which is related to the LOS velocity V_C of the cloud and the reference-line-center wavelength λ_0 via

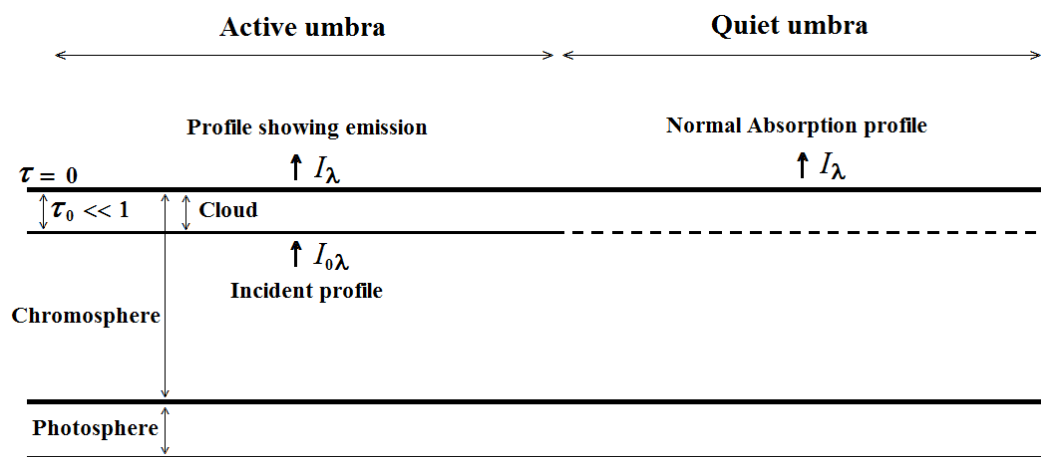


Figure 6: Geometry of the chromospheric cloud. The source function is always non-zero in active umbra but, in quiet umbra the source function has a non-zero value when an umbral flash is propagating or evolving.

$$V_C = \frac{\lambda_P - \lambda_0}{\lambda_0} c \quad (5)$$

In this relation, c is the speed of light. By the definition of τ_λ in Eq. (4), the wavelength-dependent total emission of the cloud E_λ has the same Gaussian function as τ_λ with a peak total emission of $E_0 = \tau_0 S$.

The Doppler width W depends on temperature T and micro-turbulent velocity ξ through the relationship

$$W = \frac{\lambda_0}{c} \sqrt{\frac{2k_B T}{m} + \xi^2} \quad (6)$$

where m is the atomic mass of the absorbing/emitting element and k_B is the Boltzmann constant.

The four adjustable/free parameters of the thin cloud model are the source function S , the Doppler width W , the peak optical thickness τ_0 and the LOS velocity V_C . All these parameters are assumed to be constant through the cloud structure that is responsible for the observed emission.

As mentioned before, in this work we are only interested in obtaining the Doppler velocity map in the selected big umbra (see Fig. 1) by applying the described inversion based on cloud model on Stokes I profiles of Ca II 854.2 nm. As far as the LOS velocity values are concerned, the cloud model can be used since velocity is the most model-independent parameter.

4.2 Background Incident Profile

The profile of background incident light on the cloud from below is defined as the average of normal absorption profiles in quiet umbra with the same continuum/far-wing intensity as the observed profile. This assumption is based on the fact that pixels in quiet umbra showing emission (such as pixel **a** marked in Fig. 1) show small fluctuations at their continuum/far-wing intensity during the whole observation (see the left panels of Fig. 4). Also, this fact can be seen in Figs. 4 & 5 in de la Cruz Rodriguez et al. [5] who have studied umbral flashes in a sunspot chromosphere. Also, Fig. 1 in de la Cruz Rodriguez et al. [16] who have studied a magnetic chromospheric region in quiet Sun, displays that the photospheric wings of “reversed-core” profiles of Ca II line at 854.2 nm (showing emission) are identical in brightness and shape to those of quiet region profiles that show a typical absorption shape.

By ignoring the small absorption through the upper layers of the quiet umbral chromosphere that are optically thin (see Eq. (2)), this averaged profile can be the best sample profile describing the incident profile into the cloud.

In this work, a normal absorption profile is selected by finding the curvature of the Stokes I profile around the expected position of line center; if two sets of four adjacent wavelength positions (among seven wavelength positions around the line-core) show a positive concavity, the profile can be a normal absorption profile. For more certainty, some considerations based on the equivalent line width were applied; according to the standard definition of equivalent line width, the profiles showing emission have smaller line width with respect to that of normal absorption profiles. In the case of strong emission, we obtain a negative line width.

Fig. 7 displays the histogram of line-core velocities using a parabola fit (thick black line) and center-of-gravity velocities - between the intensity level of line-core and 60% of line depth - (thick red line) for all obtained normal absorption profiles in the studied umbra. Thin solid lines in Fig. 7 show the velocity distributions of umbral profiles excluding the

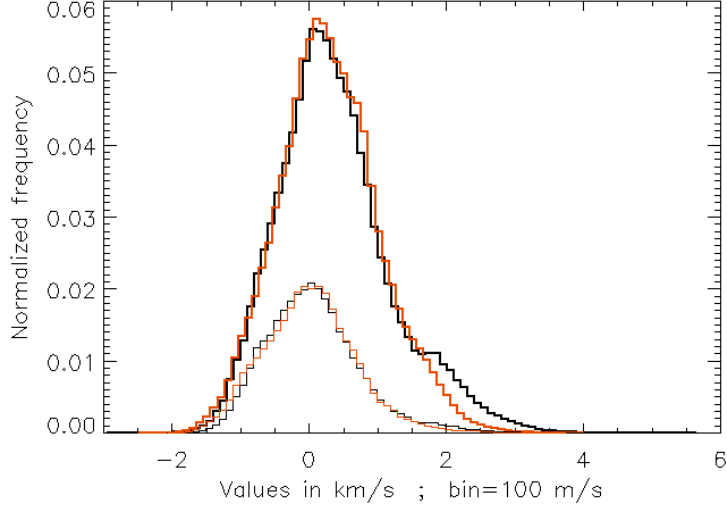


Figure 7: The histogram of core velocities (black lines) and center-of-gravity velocities (red lines) of normal absorption profiles obtained in the whole studied area (thick lines) and in the umbra (thin lines).

light bridge and penumbral parts in the studied area. As it is obvious from Fig. 7, we have adopted the peak position of the distribution of core velocities in umbra as the zero-velocity reference λ_0 .

To compute the background incident profile we make the average of 50 (at most) normal absorption profiles with the same far-wing intensity as the observed profile. To prevent an artificial line broadening, we select only normal profiles whose line-core velocities are within $\pm 700 \text{ m s}^{-1}$ (equivalent to line-core positions within $\Delta\lambda = \pm 0.02 \text{ nm}$). Then, we shift these profiles to zero-velocity reference and compute the averaged profile.

4.3 Model Fitting

Using Eq. (4), Eq. (3) can be rewritten as

$$I_\lambda - I_{0\lambda} = \tau_0 e^{-\left(\frac{\lambda - \lambda_P}{W}\right)^2} (S - I_{0\lambda}) \quad (7)$$

We use an iterative method that consists of three steps.

1) First, estimate of free parameters: at the first step, we ignore $I_{0\lambda}$ on the right hand side of Eq. (7). This assumption is reasonable since τ_0 is much less than unity. Then the value of $S - I_{0\lambda}$ on the right hand side must be large enough to adjust the difference value on the left hand side, although the position of λ_P and the value of W have important roles in this adjustment. Then, Eq. (7) is reduced to

$$I_\lambda - I_{0\lambda} = S\tau_0 e^{-\left(\frac{\lambda - \lambda_P}{W}\right)^2} \quad (8)$$

By fitting a Gaussian function to the difference profile $I_\lambda - I_{0\lambda}$, we can calculate the first estimate of two parameters λ_P and W , and an estimate for the peak total emission $S\tau_0$. Assuming an arbitrary small value for τ_0 (e.g. $\tau_0 = 0.05$) as an initial value, we obtain the first estimate of the source function S .

2) If we substitute the first estimate of S in Eq. (7), the left hand side of the following equation obeys a Gaussian function as

$$\frac{I_\lambda - I_{0\lambda}}{S - I_{0\lambda}} = \tau_0 e^{-\left(\frac{\lambda - \lambda_P}{W}\right)^2} \quad (9)$$

In this step, by finding the best fit of a Gaussian function on the difference-ratio profile (the left hand side of Eq. (9)), we calculate new values for the three free parameters τ_0 , λ_P and W . Then, at $\lambda = \lambda_P$, the new value of S can be calculated from the fitted difference-ratio profile. In this step, we calculate the sum of the squared differences between the observed Stokes I profile and the fitted one to compare the quality of the fit with the quality of the next fit.

3) Substituting the new value of S in Eq. (9), we can repeat the procedure of step (2) to obtain the best new values for all free parameters. The iteration can be repeated till we obtain the minimum value of the squared differences or the relative change of squared differences reaches less than 0.1%. This procedure is robust and in most cases, after at most five iterations, we will obtain the best fitted values.

Since the core position of the incident profile can affect the obtained LOS cloud velocity V_C , we have repeated the described iteration method using incident profiles shifted by core velocities up to 5.5 km s⁻¹, both red- and blue-shift. Then, we selected the four free parameters for the best final fit. Thereby, we introduced a new free parameter, the core velocity of the incident background profile v_{bg} . By assuming $\tau_0 = 0.05$ as an initial value for the peak optical thickness of the cloud, in the followings we describe the results of the iteration method.

Fig. 8 shows two examples of the observed profile (black solid line), the background profile (red dashed line) and the final fitted profile (green solid line) for the two sample pixels **a** in the quiet umbra (left panel) and **b** in the active umbra (right panel).

5 Results

5.1 Doppler Velocities and Line Widths

The thin cloud model described is applied only on profiles showing a spectral emission signature to obtain the LOS velocity V_C of the cloud (see Eq. (5)). However, the center-of-gravity method (between the intensity level of line-core and 60% of line depth) is applied to the profiles keeping their absorption shape, especially in the quiet umbra, to obtain an averaged Doppler velocity along the formation height of the spectral line core. Fig. 9 shows the histogram of the obtained Doppler velocities (thin lines) for all pixels, pixels without the emission signature, and those showing the emission, and the histogram of the Doppler widths (thick lines) during the whole observation.

The Doppler width of a profile without emission signature is obtained using a Gaussian fit. Black solid lines, red solid lines and green dash-dotted lines in Fig. 9, display the corresponding histograms for all pixels, pixels that do not show emission signature and those showing an emission, respectively.

The histogram of v_{bg} , the line-core velocity of the incident background profiles after finding the best fit at the end of the iteration process, is plotted in the left panel of Fig. 10. The asymmetry of this histogram is similar to the asymmetry of graphs in Fig. 7 and the thin-red-line graph in Fig. 9, which supports the correctness of our iteration procedure to obtain the best fitted parameters. The relation between v_{bg} and V_C is illustrated in the right panel of Fig. 10. A possible correlation between v_{bg} and V_C is seen in this plot. In many

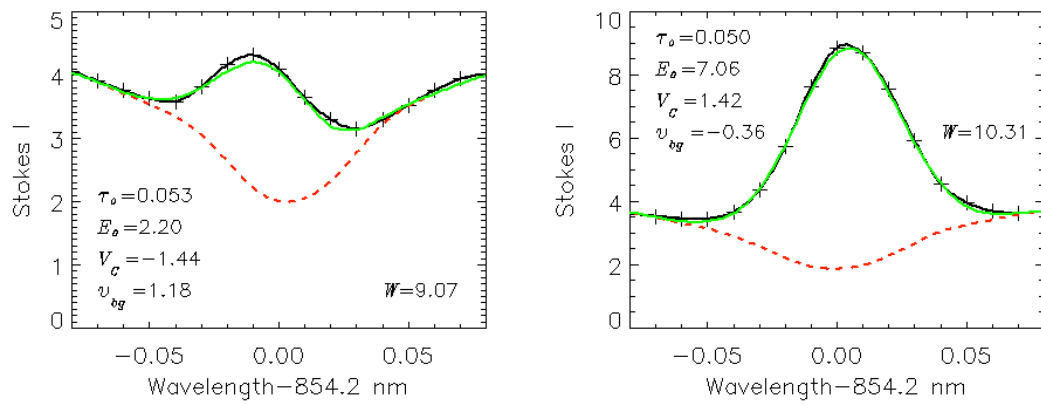


Figure 8: Examples of the observed (plus symbols and black solid line), the background profile (red dashed line) and the final fitted profile (green solid line) for two selected sample profiles: in quiet umbra (left panel; pixel **a**) and in active umbra (right panel; pixel **b**). The best fitted values of τ_0 , E_0 , V_C , v_{bg} and W are shown in each panel.

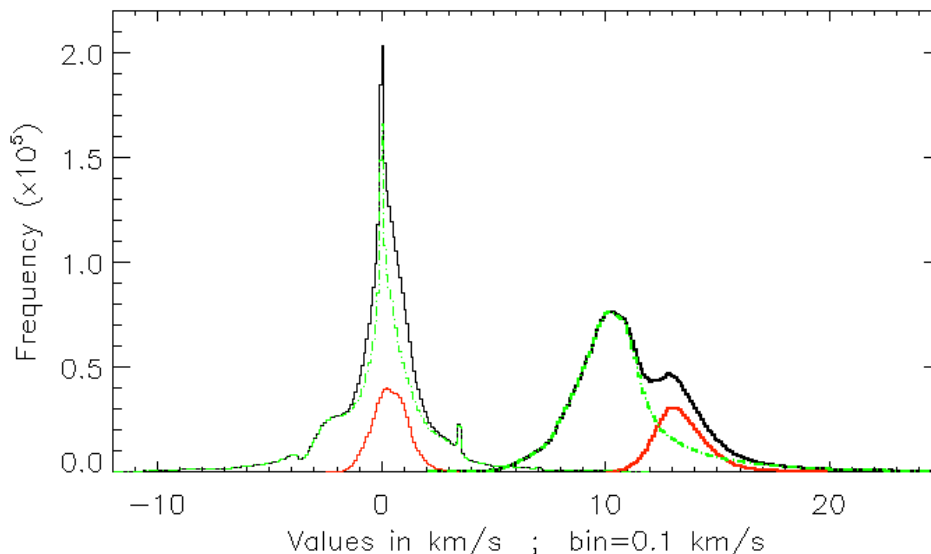


Figure 9: Histograms of the Doppler velocities (thin lines) and Doppler widths (thick lines) during the whole observation. Black solid lines, red solid lines and green dash-dotted lines display the corresponding histograms for all pixels, pixels that do not show emission signature and those showing an emission, respectively. Negative Doppler velocities correspond to upflows.

pixels, the obtained velocities reflect the propagation of waves from the photosphere to the cloud so that the photospheric and chromospheric velocities can be partially correlated.

About 0.4% of pixels show peak optical thickness $\tau_0 > 0.1$. Fig. 11 displays the histogram of the fitted τ_0 values (black solid line).

5.2 Influence of the Optical Thickness on the Results

If we change the initial value of τ_0 to a larger value 0.1 or 0.15, we will obtain similar histograms for final fitted τ_0 as shown in Fig. 11 (blue and red lines, respectively) with shifted peaks to 0.1 and 0.15, respectively, in expense of obtaining smaller source functions. However, in the case of $\tau_0 < 0.1$, values of the product $S\tau_0$ (peak total emission, E_0) for each pixel are almost the same. Fig. 12 shows the scatter plots of peak total emission (E_0) for different initial values of τ_0 versus the one-to-one correspondence of E_0 for the initial value $\tau_0 = 0.05$. In Figs. 12 & 13, we have added the results of the iteration process for the initial value $\tau_0 = 0.02$ to have a better comparison.

Fig. 13 displays the distribution of the absolute values of the differences between the obtained Doppler velocities for three sets of results of $\tau_0 = 0.05$ and $\tau_0 = 0.15$ (red line), of $\tau_0 = 0.05$ and $\tau_0 = 0.1$ (blue line) and of $\tau_0 = 0.05$ and $\tau_0 = 0.02$ (green line). The histograms have peaks around zero and quickly decrease towards larger values.

Both Figs. 12 & 13 demonstrate that there is a good solution for the radiative transfer equation based on thin cloud model (with $\tau_0 < 0.1$) for profiles showing emission. As

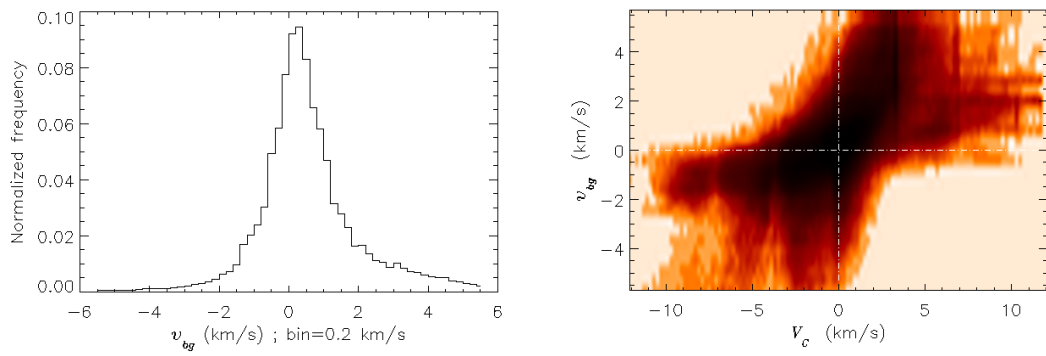


Figure 10: Left panel: the histogram of v_{bg} . Right panel: scatter plot of v_{bg} versus V_c . The color map scales the population/frequency of each point; darker region means more frequency.

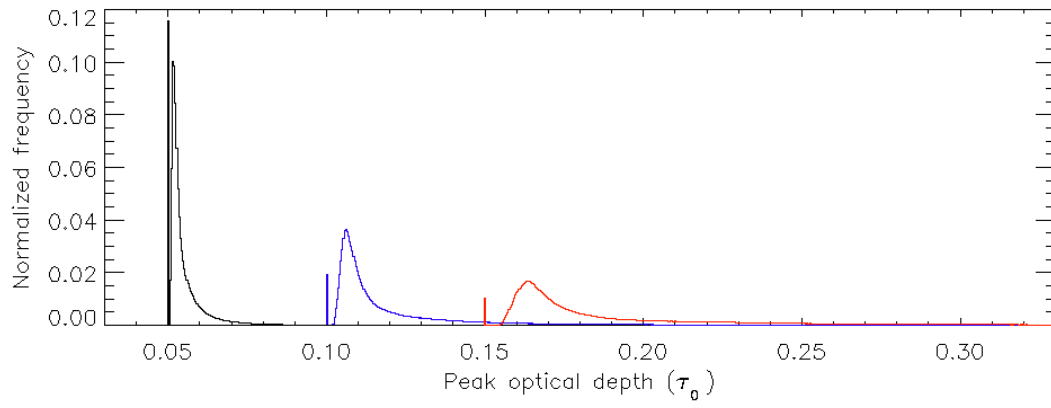


Figure 11: Histograms of the obtained peak optical thicknesses for three different initial values of τ_0 : 0.05 (black line), 0.1 (blue line) and 0.15 (red line).

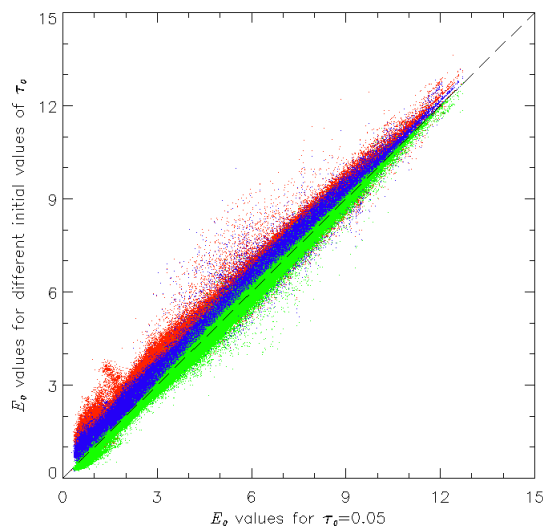


Figure 12: Scatter plots of peak total emission ($E_0 = S\tau_0$) for different initial values of τ_0 (0.1: red dots; 0.15: blue dots; 0.02: green dots) versus the one-to-one correspondence of E_0 for the initial value $\tau_0 = 0.05$.

mentioned before, the cloud Doppler velocity and its total emission are two important free parameters of the model that are practically independent of the initial value of τ_0 .

For a deep investigation of the effect of the initial value of τ_0 on other free parameters of the thin cloud model, we again consider the two pixels **a** and **b** whose spectral profiles have been shown in Fig. 8. For each one of these pixels, we change the initial value of τ_0 from 0.002 to 0.5 and compare the fitted free parameters. Figs. 14 & 15 show the changes of the fitted free parameters of the model E_0 , V_C and W versus the final fitted for pixels **a** and **b**, respectively. As seen from these figures, assuming $\tau_0 < 0.1$ as an initial value for optical thickness of the cloud, the thin cloud model retrieves unique values for other free parameters of the model.

5.3 Examples of Line-profile Fits

For a better illustration of the efficiency of thin cloud model to retrieve atmospheric physical parameters, some pixels with different spectral profiles from two vertical cuts, one in the quiet umbra when an umbral flash is seen and the other in the active umbra at the same time, were selected. The fitted profiles and their corresponding atmospheric physical parameters are given in Figs. 16 & 17, respectively. Top middle panel in Fig. 16 shows an observed profile with a typical absorption shape that does not show emission signature. This profile shows a center-of-gravity velocity V_{cog} of 1.1 km s^{-1} .

6 Conclusions

According to the results of the solution of the radiative transfer equation based on thin cloud model, we can compare the dynamical atmospheric parameters of quiet and active umbra; the active umbra shows a steady emission in Ca II 854.2 nm line as well as in H α line, with a high source function and equivalently, with a large peak total emission, as can be seen in

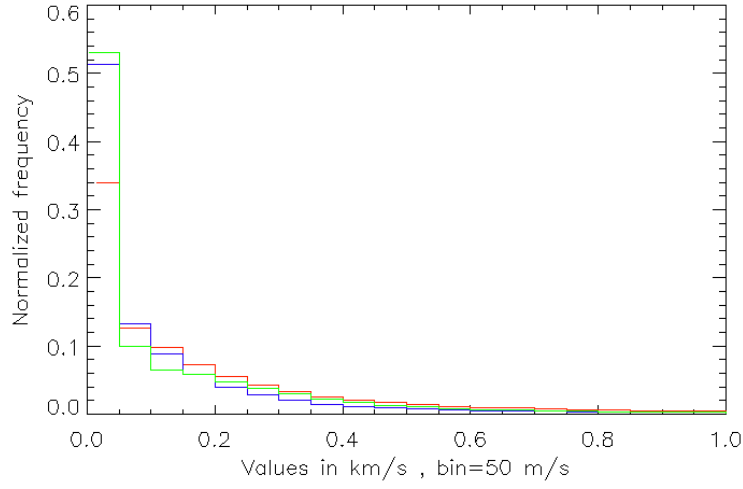


Figure 13: Histograms of the absolute values of differences between the obtained Doppler velocities for two different initial values of peak optical thickness: red line for $\tau_0 = 0.05$ and $\tau_0 = 0.15$; blue line for $\tau_0 = 0.05$ and $\tau_0 = 0.1$; green line for $\tau_0 = 0.05$ and $\tau_0 = 0.02$.

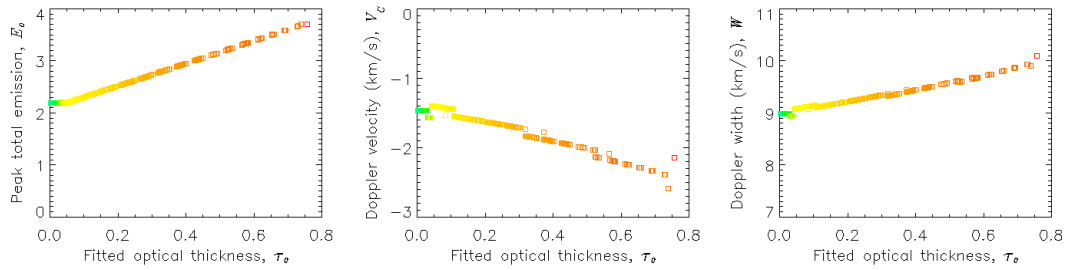


Figure 14: Changes of the fitted free parameters of thin cloud model E_0 , V_C and W versus the final different fitted τ_0 for the pixel **a** in the quiet umbra. The colored squares scale the squared differences value of the fitted profile and of the observed profile from minimum value (the best fit, green) to maximum value (the worst fit, red).

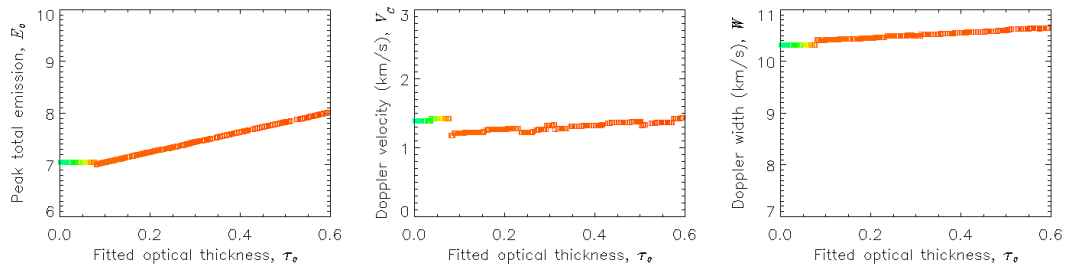


Figure 15: Same as in Fig. 14 but for the pixel *b* in the active umbra.

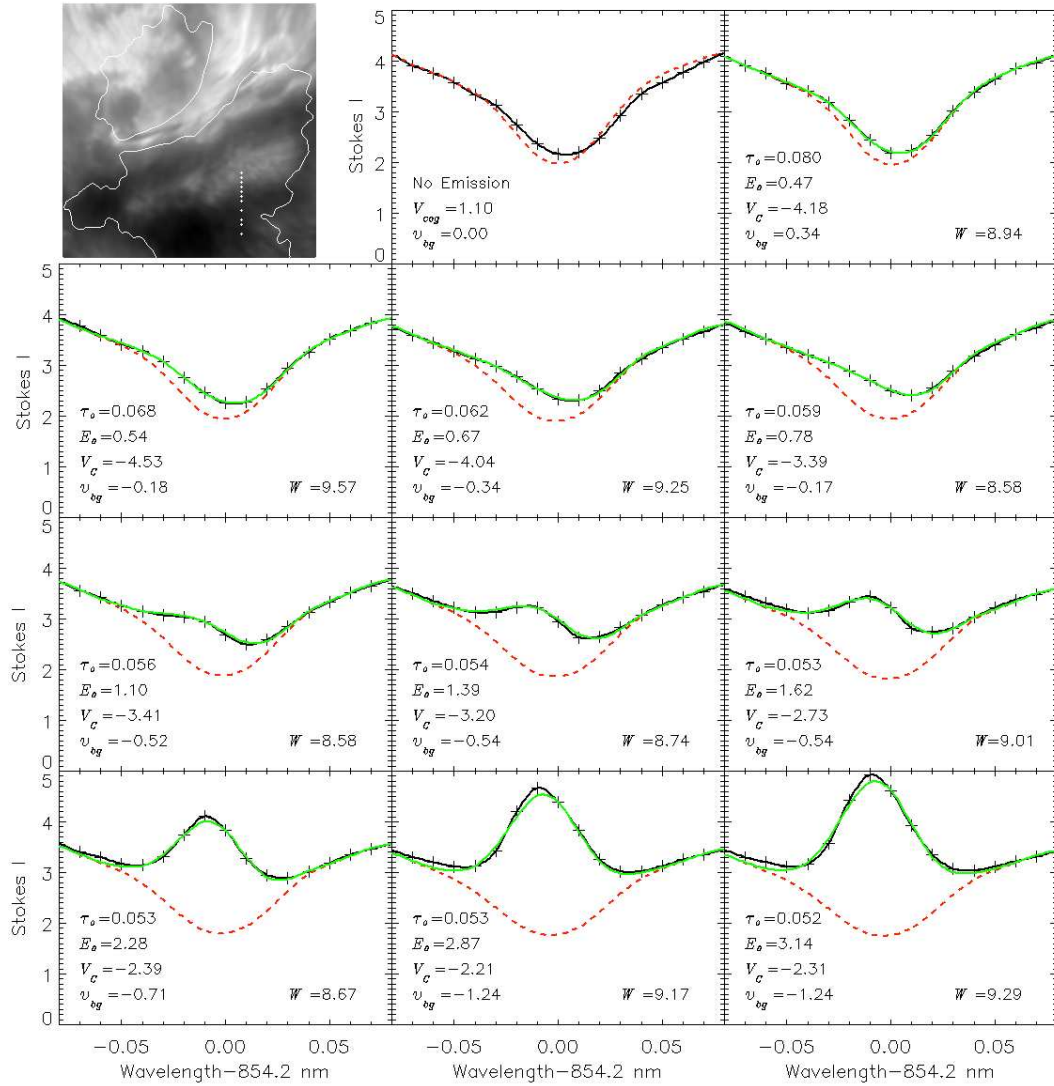


Figure 16: Different spectral profiles from a vertical cut (white small plus symbols in top-left panel: line-core filtergram of the third scan) in the quiet umbra when an umbral flash is seen. Observed profile: plus symbols and black solid lines; background incident profile: red dashed lines; fitted profiles: green solid lines. The lowest white plus symbol in top-left panel corresponds to the top-middle panel and the highest white plus symbol corresponds to the bottom-right panel.

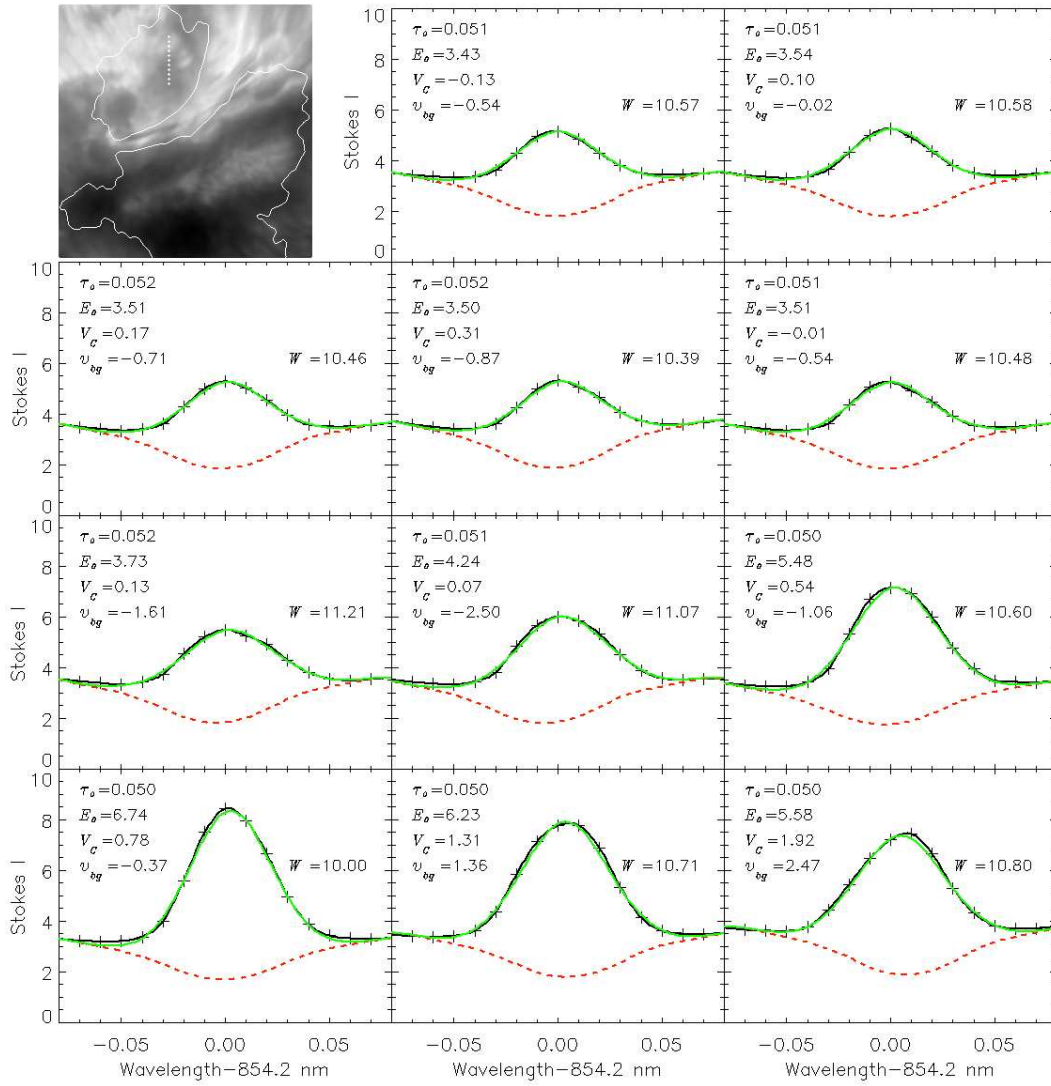


Figure 17: Same as in Fig. 16 but for different spectral profiles from a vertical cut (plus symbols in top-left panel) in the active umbra.

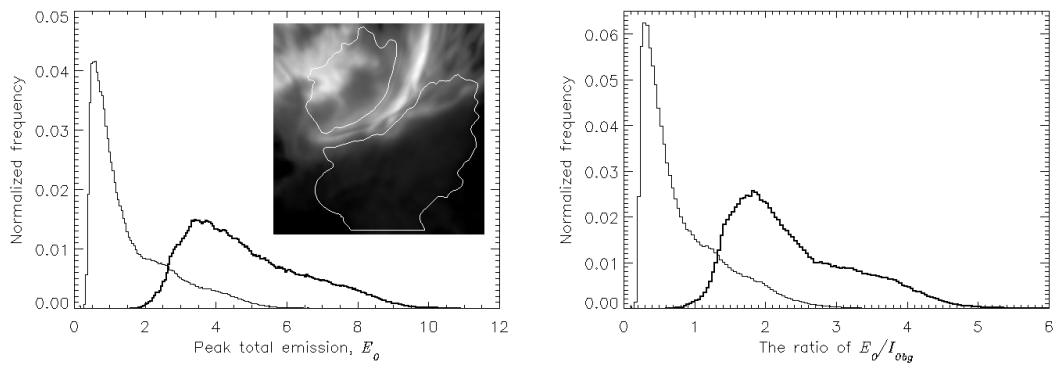


Figure 18: Left panel: histograms of the peak total emission E_0 in the quiet umbra (thin solid line) and in the active umbra (thick solid line). The inset image is the time average of E_0 . Pixels in quiet and active umbra used to construct the histograms are enclosed by white contours. Right panel: corresponding histograms of the ratios of the peak total emission E_0 to the corresponding line-core intensity of the incident background profile I_{0bg} in both active (thick solid line) and quiet umbra (thin solid line).

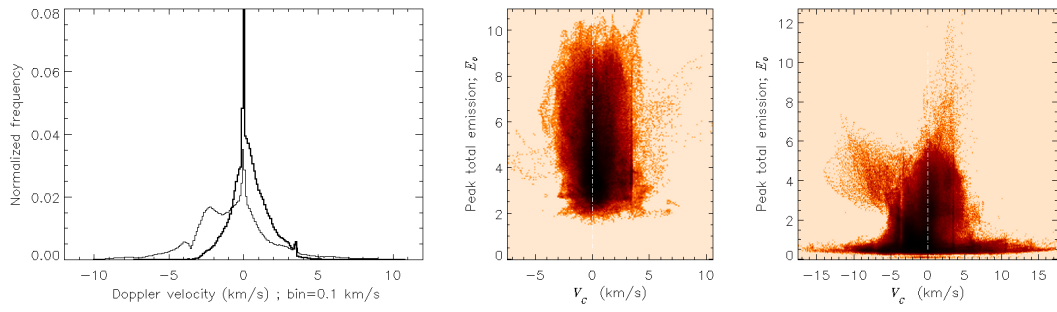


Figure 19: Left panel: histograms of Doppler velocities (V_C) in the quiet umbra (thin solid line) and in the active umbra (thick solid line). Negative Doppler velocities show up-flows. Middle panel: scatter plot of E_0 versus V_C for the active umbra. Right panel: scatter plot of E_0 versus V_C for quiet umbra. The color map scales the population/frequency of each point; darker region means more frequency. Pixels in the quiet and active umbra used to construct the histograms and scatter plots are the same as those defined in Fig. 18.

the left panel of Fig. 18. On the other hand, pixels inside the quiet umbra show emissions only when an umbral flash is propagating through the umbra. During the propagation of an umbral flash, the peak total emission of pixels inside the quiet umbra varies from smaller values accompanied by higher upflows to larger values with smaller up- or downflows. The temporal and spatial averages of the peak total emission in the quiet and active umbra are about 1.54 and 4.82, respectively. The right panel of Fig. 18 displays histograms of the ratio of the peak total emission E_0 to the corresponding line-core intensity of the incident background profile I_{0bg} in both active (thick solid line) and quiet umbra (thin solid line). These distributions are similar to the corresponding distribution of E_0 . This ratio gives us a measure showing how large is E_0 and how strong is the spectral emission.

Histograms of resulting Doppler velocities are shown in Fig. 19 (left panel). It can be seen from the figure that while upflows are dominant in the quiet umbra, the active umbra is connected mostly with downflows.

The scatter plot of E_0 versus V_C for the quiet umbra (right panel of Fig. 19) shows two different parts: very large values of E_0 are related to downflows with Doppler velocities less than 5 km s^{-1} ; while, a considerable population of pixels with moderate $E_0 (< 7)$ shows upflows with large Doppler velocities up to 15 km s^{-1} . A detailed description of the obtained velocity maps and the possible interpretation of the velocity distributions will be discussed elsewhere.

Acknowledgment

H. Hamedivafa thanks the Imam Khomeini International University for supporting his sabbatical stay at the Astronomical Institute of the Czech Academy of Sciences. The work was also supported by the Czech Science Foundation under the grant 14-04338S. The Swedish 1-m Solar Telescope is operated on the island of La Palma by the Institute for Solar Physics of Stockholm University in the Spanish Observatorio del Roque de los Muchachos of the Instituto de Astrofísica de Canarias. We acknowledge financial support by the Spanish Ministerio de Economía y Competitividad through projects AYA2012-39636-C06-05 and ESP2013-47349-C6-1-R, including a percentage from European FEDER funds. Also, H. Hamedivafa thanks P. Heinzel and J. Štepan for their helpful discussions and suggestions.

References

- [1] Beckers, J., M., & Tallant, P., E., 1969, Sol. Phys. 7, 351
- [2] Socas-Navarro, H., et al., 2000, Science 288, 1396
- [3] Rouppe van der Voort, et al., 2003, A&A 403, 277
- [4] Khomenko, E., & Collados, M., 2015, Living Rev. Solar Phys. 12, Irsp-2015-6
- [5] de la Cruz Rodríguez, J., et al., 2013, A&A 556, 115
- [6] Socas-Navarro, H., et al., 2000, ApJ 544, 1141
- [7] Beckers, J., M., 1964, “A Study of the Fine Structures in the Solar Chromosphere”, PhD thesis, Univ. Utrecht
- [8] Tziotziou, K., 2007, in ASP Conf. Ser. 368, The Physics of Chromospheric Plasmas, eds., P., Heinzel, I., Dorotovic, & R., J., Rutten, San Francisco, CA: ASP, 217

- [9] Alissandrakis, C., E., et al., 1990, A&A 230, 200
- [10] Tsiropoula, G., et al., 1993, A&A 271, 574
- [11] Scharmer, G., B., 2006, A&A 447, 1111
- [12] Scharmer, G., B., et al., 2003, “The 1-meter Swedish Solar Telescope” in Innovative Telescopes and Instrumentation for Solar Astrophysics, eds., S., Keil & S., Avakyan, Proc. SPIE, 4853, 341-350
- [13] de la Cruz Rodríguez, J., et al., 2015, A&A 573, 40
- [14] Cauzzi, G., et al., 2008, A&A 480, 515
- [15] Heinzel, P., & Schmieder, B., 1994, A&A 282, 939
- [16] de la Cruz Rodríguez, J., et al., 2013, ApJ 764, L11